Journal of Materials Chemistry A

Accepted Manuscript

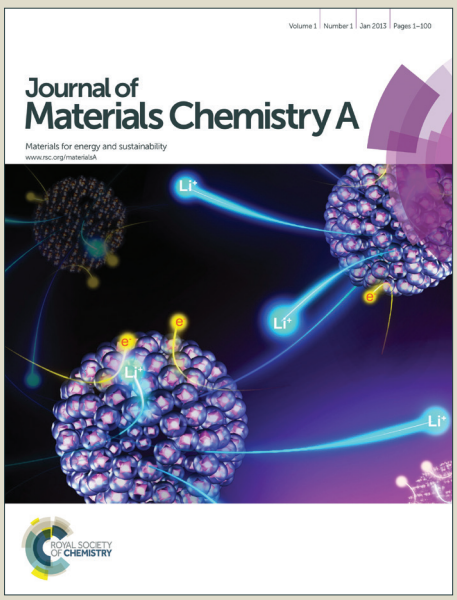

ROYAL SOCIETY OF CHEMISTRY

www.rsc.org/materialsA

Cite this: DOI: 10.1039/c0xx00000x

www.rsc.org/xxxxxx

paper

A new-type semiconductor $Na_{0.9}Mg_{0.45}Ti_{3.55}O_8$: preparation, characterization and photocatalysis

Ze-Qing Guo,[a] Jian-Ping Zhou,*[a] Long-Liang An,[a] Jia-Xing Jiang,[b] Gang-Qiang Zhu,[a] Chao-Yong Deng[c]

Received (in XXX, XXX) Xth XXXXXXXXX 20XX, Accepted Xth XXXXXXXXX 20XX

DOI: 10.1039/b000000x

A new-type semiconductor photocatalyst $Na_{0.9}Mg_{0.45}Ti_{3.55}O_8$ (NMTO) was prepared by a simple hydrothermal method for the first time. NMTO single crystal nanosheets with dominant {0 0 1} facets were obtained at 300 °C with 1 M NaOH over 40 min. HRTEM and XPS analyses confirmed the well crystallized nanosheets. NMTO was demonstrated as a direct semiconductor with a band gap of about 3.55 eV. Pure NMTO exhibited high photodegradation ability for methylene blue (MB) under UV-visible light irradiation even considering the surface area. The trapping experiments indicated that the photogenerated holes were mainly responsible for the MB photodegradation. The presence of H_2O_2 significantly improved the photocatalytic activity of NMTO by inhibiting the electron-hole recombination through capturing the photogenerated electrons. A possible mechanism for the photodegradation of MB over NMTO is proposed. This work highlights the potential application of NMTO in the field of energy conversion.

Introduction

Environmental pollution with various chemical compounds has become a serious issue with the rapid development of modern industry. In the past few decades, many efforts have been devoted to search efficient photocatalysts for pollutant decomposition under solar energy. Semiconductor photocatalysis is a promising approach toward solving the worldwide environmental and energy issues. Titanium dioxide (TiO_2) has been proven as one of the most versatile photocatalyst because of its high catalytic activity, long-term stability, strong optical absorption, low cost and environmental friendliness.[1,2] Both theoretical and experimental researches about TiO_2 polymorphs indicated that the metastable {0 0 1} facets of anatase showed higher reactivity than the others.[3,4] Then, the effect of TiO_2 surface on the photocatalytic performance has been intensively explored at the atomic level, including {0 0 1}, {0 1 0}, {1 0 1} facets,[5-8] even high-index {1 0 5} facets.[9] Unfortunately, the surfaces with high reactivity usually diminish rapidly during the crystal growth due to the minimization of surface energy, and the photoefficiency of TiO_2 is substantially limited by its usually fast electron-hole recombination. Many efforts have been made to improve the photocatalytic activity of the TiO_2-based materials. Non-stoichiometric TiO_2 was developed to enhance the photocatalytic activity.[10,11] Ion doped TiO_2 can suppress the recombination of photogenerated charge carriers.[12-15] Binary oxides, especially bismuth titanate, can improve the photocatalytic activity by adjusting the surface activity.[16,17] The Schottky junction by combining TiO_2 nanoparticles and noble metals[18,19] and the composite based on TiO_2[20] are also effective methods to inhibit the recombination of photogenerated charge carriers.

It is desirable to develop novel photocatalysts with higher photocatalytic activity, good stability, and low cost to achieve an economically and environmentally acceptable photocatalysis process. $Na_{0.9}Mg_{0.45}Ti_{3.55}O_8$ (NMTO) is free of toxicity and heavy element as one of the TiO_2-based compounds, which are competitive candidates in photocatalytic applications. Unfortunately, the chemical and physical properties of this compound have NOT been explored since it was firstly synthesized by a solid state reaction method in 1989.[21] Herein, we report the photocatalytic activity of NMTO nanosheets synthesized via a simple hydrothermal method. NMTO exhibits a superior photocatalytic reactivity to TiO_2 on the degradation of dye methylene blue (MB), indicating that NMTO is a promising semiconductor photocatalyst for pollutant decomposition.

Experimental details

NMTO Synthesis

NMTO nanosheets were prepared by a hydrothermal method under different experimental conditions. The chemicals titanium dioxide (98%), light magnesium oxide (98.5%) and sodium

hydroxide (96%) were used as received without further purification. In a typical procedure, MgO and TiO_2 with $Na_{0.9}Mg_{0.45}Ti_{3.55}O_8$ stoichiometry were added into 120 mL of NaOH aqueous solution with different alkaline concentrations under stirring for 30 min. Subsequently, the ivory mixture was transferred into a 150 mL stainless steel autoclave, sealed and heated up to different temperatures for hydrothermal treatment under mechanical stirring, and finally cooled down to room temperature naturally. The sample was collected and washed by distilled water and ethanol. The product was dried at 80 °C for 24 h.

Characterization

The crystal structure of the as-synthesized powders was identified by X-ray powder diffraction (XRD) using a D/Max2550 X-ray diffractometer (Rigaku, Japan) with Cu Kα radiation (λ =1.5406 Å). The samples were measured at a scanning rate of 5 °/min in the 2θ range of 10 – 70° under 40 kV and 100 mA. The morphology of the samples was characterized by a field emission scanning electron microscopy (FESEM, Hitachi, S-4800) with an accelerating voltage of 20 kV. The crystalline characteristics of the NMTO nanosheets were determined by a high-resolution transmission electron microscopy (HRTEM) and selected-area electron diffraction (SAED, Tecnai G^2F20 S-TWIN) with an accelerating voltage of 200 kV. Energy Dispersive X-Ray Spectroscopy (EDX) was employed to determine the Na, Mg, Ti, O element ratio in the products. For HRTEM sample preparation, the powders were suspended in ethanol, and a drop of this suspension was deposited on a holey carbon film supported by a copper grid. Then, HRTEM specimen was dried in air before the HRTEM measurement. UV-vis absorption spectra were measured under the diffuse reflection mode with a Lambda 950 UV-VIS-NIR spectrophotometer (Perkin-Elmer, USA) in the wavelength range of 200-800 nm. Specific surface areas of the samples were measured with N_2 adsorption-desorption isotherms at 77 K in a Micromeritics ASAP 2010 system after the samples were preheated at 120 °C for 12 h in vacuum. The surface area was calculated using the Brunauer-Emmett-Teller (BET) method. X-ray photoelectron spectroscopy (XPS) was performed on an ESCALAB MKII X-ray photoelectron spectrometer (VG Scientific, UK) using Al Kα radiation for the chemical analysis.

Photodegradation measurement

The photocatalytic activity of the NMTO nanosheets was characterized by the photodegradation rates of organic pollutant dye MB. The measurement was executed with UV-visible light generated by a 400 W tungsten halogen lamp (simulated sunlight). The NMTO catalyst was dispersed in a 60 mL quartz tube containing 50 mL of MB aqueous solution, which was maintained at 15 °C by water flowing through a cooling jacket of the reactor. The concentration of NMTO catalysts is 1.0 g/L while the initial concentration of MB is 20 mg/L. The mixture was ultrasonicated for 30 min followed by stirring for 30 min in dark to ensure an adsorption-desorption equilibrium. The mixture was then irradiated by the tungsten halogen lamp to start the MB photodegradation. During irradiation, the tubes were placed on the carousel inside the photoreactor to ensure the equal exposure of each tube in the tungsten halogen lamp light. The mixture was magnetically stirred during the reaction. After a certain time interval, 2 mL suspension was taken out for MB concentration analysis. The MB concentration was monitored by recording the characteristic absorption peak of MB (664 nm) with a U-3010 UV-vis spectrophotometer (Hitachi, Japan).

Results and discussions

Structural analysis

Fig. 1a shows the XRD patterns of the samples hydrothermally treated for 80 min with 1 M NaOH at different temperatures. The powder reacted at 260 °C is anatase TiO_2 (JCPDS No. 78-2486). When the reaction temperature increases to 280 °C, NMTO appears though TiO_2 is still the main phase. Pure NMTO is obtained at the higher temperatures of 300 °C and 320 °C. The diffraction peaks are from monoclinic NMTO (JCPDS No. 44-0007, S.G.: C2/m) with lattice parameters of a = 1.2270 nm, b = 0.3812 nm, c = 0.6487 nm, and β = 107.33°. The XRD patterns of the samples synthesized at 300 °C for 80 min with different NaOH concentrations are shown in Fig. 1b. The content of NMTO increases with the NaOH concentration, and pure NMTO is obtained with the NaOH concentration of over 1 M.

It is worth to change the reaction time to reveal the NMTO formation process on the basis of above experimental results. Fig. 1c exhibits the XRD patterns of the samples synthesized at 300 °C and 1 M NaOH for different reaction times. NMTO appears in the powder after being hydrothermally treated for 20 min and NMTO powder is obtained over 40 min. These provide information to probe the reaction mechanism although the detailed process is unclear in the hydrothermal reaction. NaOH plays dual roles in the reaction process, providing an alkaline environment and natrium ion source. The Mg and Na ions enter to TiO_2 lattice under alkaline environment, high temperature and high pressure, resulting in that anatase TiO_2 changes into monoclinic NMTO.

One weak diffraction peak at 18.7° appears in the XRD pattern for part samples, which is attributed to $Mg(OH)_2$. Thus, we reduced MgO raw material by 10 wt% and 12 %. The sample with decreasing 10 wt% MgO still contains a little $Mg(OH)_2$ and that with decreasing 12 wt% MgO is indexed as pure NMTO as shown in Fig. 1d. Therefore, we prepare samples with the reduction of 12% MgO at 300 °C for 40, 60 and 80 min for comparison. They all are single phase monoclinic NMTO.

There is no report about NMTO preparation and property since it was firstly synthesized by a solid state reaction method in 1989 [21]. Herein, we successfully synthesize pure NMTO by a simple hydrothermal reaction with lower alkaline concentration. This allows us to have a deep research on it.

We select the samples hydrothermally reacted for 40, 60 and 80 min to have a detailed research for their relative pure phase.

They are signed as NMTO-I40, NMTO-I60 and NMTO-I80 according to the target temperature (Fig. 1c), respectively. Relatively, NMTO-II40, NMTO-II60 and NMTO-II80 denote the samples synthesized by reduction of 12% MgO after hydrothermal reaction of 40, 60 and 80 min (Fig. 1d), respectively.

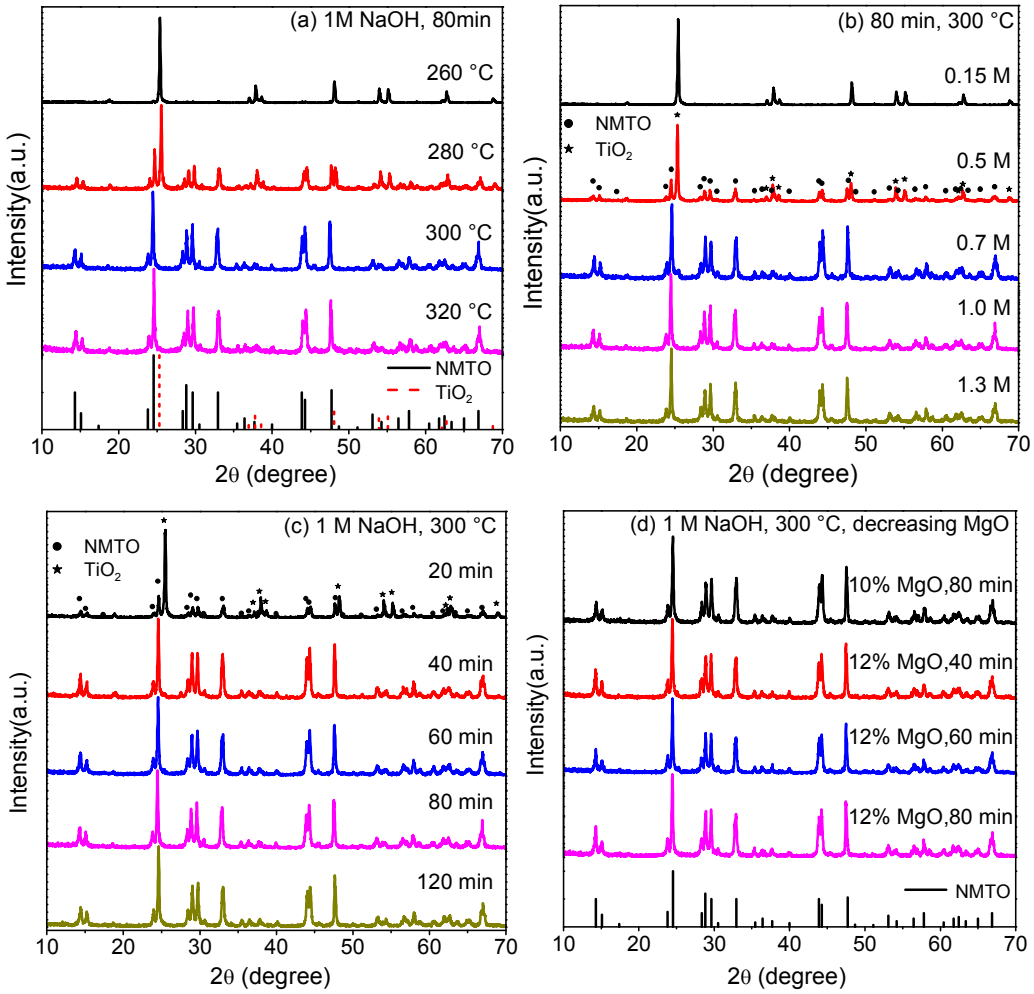

Fig. 1. XRD patterns of NMTO powders synthesized by hydrothermal method (a) at 1 M NaOH for 80 min with different temperatures, (b) at 300 °C for 80 min with different alkaline concentrations, (c) at 1 M NaOH, 300 °C for different reaction times, and (d) at 1 M NaOH, 300 °C for different reaction times with reducing MgO reagent.

Morphological characterization

Fig. 2a ~ 2c illustrate the typical HRSEM images of NMTO-I samples synthesized at different reaction times of 40, 60 and 80 min. The monoclinic NMTO nanosheets exhibit long hexagonal plate shape with typical size of about 1.0 μm in length, 450 nm in width and 40 nm in thickness. When decreasing the MgO reagent, NMTO-II nanosheets reduce size but keep the same shape as shown in Fig. 2d ~ 2e.

TEM and HRTEM were used to provide further insight into the microstructure of the long hexagonal plate. Fig. 3a presents a typical TEM image of the long hexagonal crystal. The HRTEM image in Fig. 3b, recorded along the [0 0 1] zone axis of the long hexagonal crystallite at the top of nanosheet in Fig. 3a, shows three sets of lattice stripes with spacings of 0.36, 0.36 and 0.58 nm, which are assigned to (1 1 0), $(1\,\bar{1}\,0)$ and (2 0 0) planes, respectively. The three crystal planes are parallel to the two short edges and one long edge in the nanosheet, respectively. The angles are 72°, 72° and 36° between (2 0 0) and $(1\,\bar{1}\,0)$, (2 0 0) and (1 1 0), (1 1 0) and $(1\,\bar{1}\,0)$, which are identical to the theoretical value in the crystal NMTO. The corresponding SAED image in Fig. 3c confirms the crystal characteristics. Fig. 3d shows the HRTEM image taken from one side face of the nanosheet, in which the lattice stripes with spacing of 0.62 nm is indexed as (0 0 1) plane. The stripes in the area indicated by a yellow arrow exhibit a distorted characteristic, resulting from the common boundary between (1 1 0) facet and (2 0 0) facet. The corresponding SAED pattern in Fig. 3e shows the image recorded along the [1 0 0] zone axis. The clear HRTEM crystal strips and periodic SAED patterns meet the single crystalline nature of the nanosheets. The long hexagonal plate with well defined crystalline facets has been prepared and a schematic illustration of the crystal orientation for the NMTO nanosheet is put forward in Fig. 3f based on the above results. The EDX analysis in Fig. 3g shows four elements of Na, Mg, Ti and O in the plate and the

atomic ratio is well close to the stoichiometic $Na_{0.9}Mg_{0.45}Ti_{3.55}O_8$, confirming that the well single crystal MMTO has been obtained.

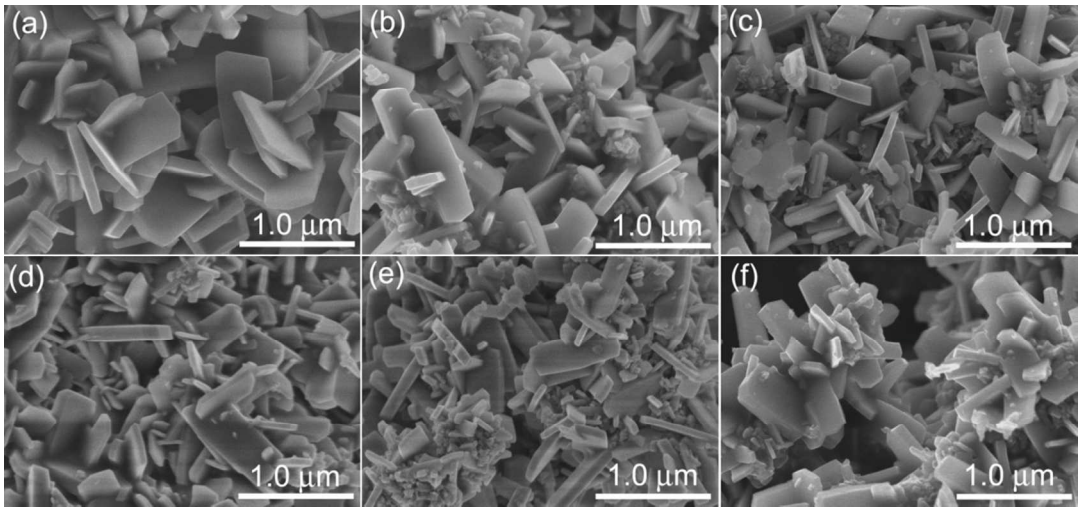

Fig. 2. Typical HRSEM images of NMTO samples synthesized at 300 °C with 1 M NaOH, (a) ~ (c) different reaction times of 40, 60 and 80 min; (d) ~ (f) different reaction times of 40, 60 and 80 min with reducing MgO reagent by 12%.

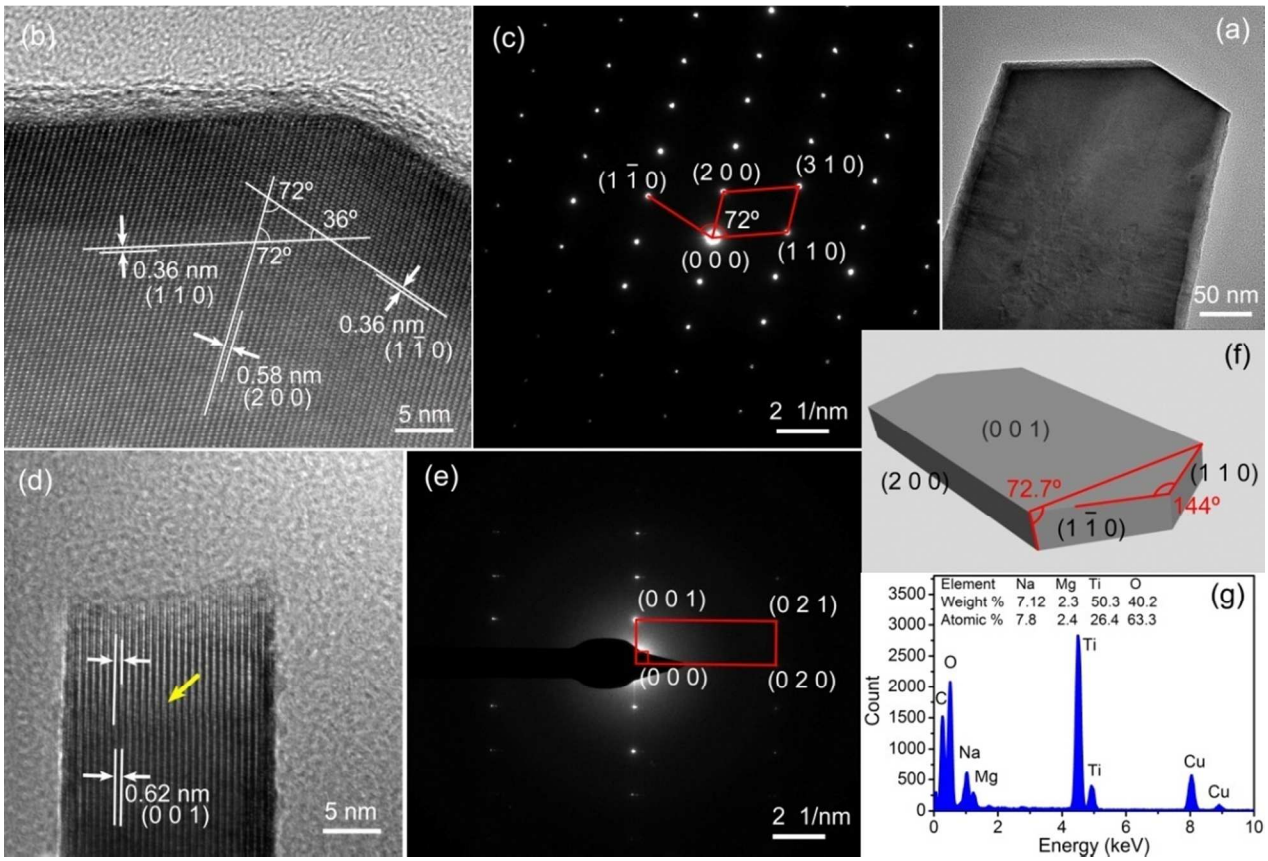

Fig. 3. (a) Typical TEM image of NMTO-II80 nanosheet; (b) HRTEM image and (c) corresponding SAED pattern taken from the top nanosheet in (a); (d) HRTEM image and (e) corresponding SAED pattern taken from one side of the nanosheet in (a); (f) schematic illustration of the NMTO nanosheet with defined facets; (g) EDX spectrum of the NMTO nanosheet.

XPS analysis

XPS was employed for the chemical analysis of NMTO-II samples. C1s peak at the binding energy of 284.6 eV, which was from CO_2 at the powder surface, was used to scale the spectra. The binding spectra are presented in Fig. 4a-4d, where the binding peaks are fitted by Lorentzian-Gaussian functions. The observed binding energies of Na1s, Mg2p, Ti2p and O1s are 1071.4, 49.3, 458.5 and 529.8 eV, which are corresponding to the

positive ions Na^{+}, Mg^{2+}, Ti^{4+} and negative ion O^{2-}, respectively. The peak profiles except that of O1s are well consistent with the standard spectra.[22] In O1s XPS spectra, two binding energy peaks appear at 531.9 and 533.4 eV besides that at 529.8 eV from the NMTO samples. The former two peaks are attributed to the oxygen from CO_2 and O_2 adsorbed on the powder surface. The XPS results further confirm the well crystallite NMTO.

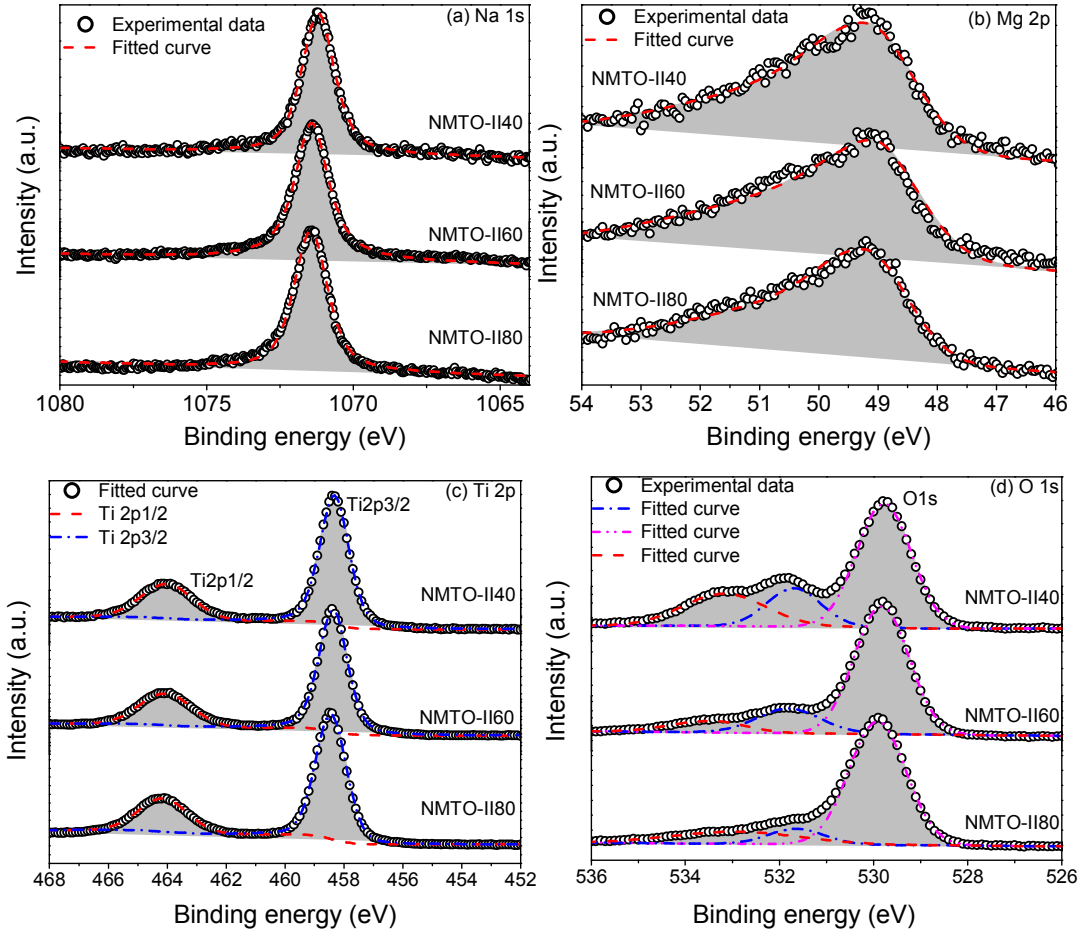

Fig. 4. (a) Na1s, (b) Mg2p, (c) Ti2p and (d) O1s XPS spectra of NMTO-II samples. The binding energies of Na1s, Mg2p, Ti2p and O1s are 1071.4, 49.3, 458.5 and 529.8 eV, respectively. The gray area indicates fitted summation.

Photophysical properties

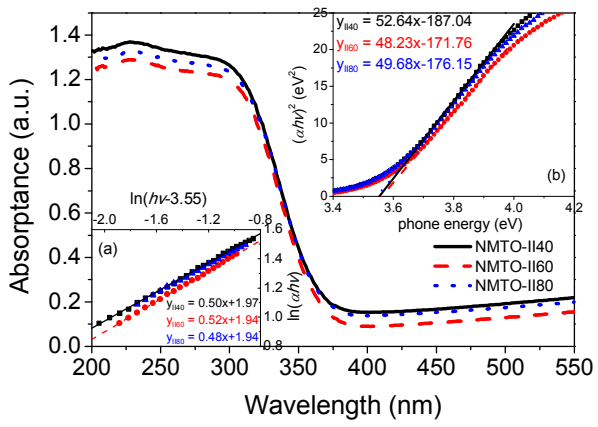

Fig. 5. UV–vis diffuse reflectance spectra of NMTO-II samples. Inset (a) plots ln($\alpha h\nu$) versus ln($h\nu$-3.55), exhibiting a direct transition; inset (b) illustrates Kubelka–Munk function against photon energy $h\nu$ to calculate the band gap. The equations are linearly fitted.

The optical properties of the NMTO samples were studied by UV-vis diffuse reflectance spectroscopy and the spectra were plotted in Fig. 5. The absorption edge at about 340 nm has a little difference, which is due to the quantum size effect,[23-25] resulting from the different crystal size as observed in the HRSEM results. It is well known that the optical absorption near the band edge follows the relation [26]

$$\alpha h\nu = A(h\nu - E_g)^{n/2} \quad (1)$$

where α, ν, A and E_g are the absorption coefficient, light frequency, proportionality constant and band gap energy, respectively. n depends on the characteristics of the transition in a semiconductor, i.e., direct transition (n = 1) or indirect transition (n = 4). We plot ln($\alpha h\nu$) as a function of ln($h\nu$ - E_g) and employ an approximate value of E_g (=3.55 eV) to determine the value n with the slope of the straightest line near the band edge. The value n for NMTO is determined as 1 from the inset (a) in Fig. 5, meaning the optical transition is directly allowed. The square of absorption coefficient is linear with energy for direct optical transition in the absorption edge region. The band gap can be

estimated by the Kubelka–Munk method. We plot $(\alpha hv)^2$ dependence on photon energy hv as shown as the inset (b) in Fig. 5. An extrapolated line of the absorbance is derived from the high slope region of the spectra.[27] Then, the band gap is determined as about 3.55 eV by the intercept of the extrapolated line to the hv axis and is listed in Table 1. This is larger than the band gap of TiO_2 (3.2 eV).

Table 1 Typical parameters of TiO_2, NMTO-II40, NMTO-II60 and NMTO-II80.

Samples	S_{BET} (m^2/g)	Band gap (eV)	Photocatalytic activity (MB)	
			k (min^{-1})	k/S_{BET} [g/(m^2·min)]
TiO_2	16.29	3.2	0.01687	1.036×10^{-3}
NMTO-II40	26.60	3.553	0.05584	2.099×10^{-3}
NMTO-II60	30.36	3.561	0.06594	2.172×10^{-3}
NMTO-II80	28.59	3.546	0.06007	2.101×10^{-3}

Photocatalytic activity

The photocatalytic performance of NMTO was evaluated in terms of the decomposition rate of MB in an aqueous solution under UV-visible light irradiation (a simulated sunlight irradiation). Fig. 6a shows temporal absorption changes of MB aqueous solution in the presence of NMTO-II60 after photodegradation reaction. The MB concentration decreases about 80% in 20 min, and the MB characteristic peak at 664 nm disappears in 40 min, indicating that MB photodegradation has almost finished.

The photodegradation profiles of C/C_0 are shown in Fig. 6b, where C_0 is the initial MB concentration after adsorption-desorption equilibrium, and C is the corresponding concentration after a specific reaction time. The MB photodegradation over TiO_2 is also measured for comparison. TiO_2 is commercially supplied with 64% rutile and 36% anatase determined by XRD. A rapid decrease in the MB concentration is realized in the presence of the NMTO-II samples. MB is almost completely photodegraded over NMTO-II60 in 40 min, similar result was obtained for NMTO-II80 and NMTO-II40. For NMTO-II60 and NMTO-II80 samples, the total MB photodegradation reaches 98% after 50 min UV-visible irradiation, while 40% MB remains after reaction by TiO_2. In addition, MB is not obviously photodegraded when it is exposed to UV-visible light without the photocatalyst or with the photocatalyst before irradiation. In other words, the MB molecule is stable under UV-visible light irradiation. Therefore, NMTO enjoys strong photocatalytic activity in MB degradation.

The pseudo-first-order model is applied to further investigate the kinetics of NMTO photocatalytic reactions, expressed as [28]

$$-\frac{dC}{dt} = kC \quad \text{or} \quad -ln\left(\frac{C}{C_0}\right) = kt \qquad (2)$$

where k is the pseudo-first reaction order rate. This model has been widely used for photocatalysis when the initial concentration of pollutant is low.[29,30] Fig. 6c shows the photocatalytic experiments on logarithmic scales. The linear trend in these plots proves that the photocatalytic degradation of MB follows the pseudo-first-order kinetics. Thus, the reaction rate k can be calculated by the linearly fitted slope as listed in Table 1. The photocatalytic activity of NMTO samples is about four times higher than that of TiO_2 based on the above data. Then, the degradation rate of MB over the samples can be placed in the following sequence: NMTO-II60＞NMTO-II80＞NMTO-II40＞TiO_2. What's more, the degradation ability of MB over NMTO is much stronger in comparison with that of the other single phase materials, such as hollow TiO_2 microspheres,[5] TiO_2 nanobelts and nanoshperes,[7] B, Ag-doped TiO_2,[13] Binary oxides,[16,23] even silver modified TiO_2 nanofibers.[18] The strong photocatalytic activity of NMTO maybe attribute to the NMTO complex crystal structure, though whose detailed crystal information is unknown so far and is desired to explore. NMTO exhibits strong photocatalysis although its large band gap limits the utilization of solar energy. On the other hand, this provide a wide space to improve the NMTO photocatalysis. We believe that the heterostructure based on NMTO or element doping could enhance the photocatalytic activity by adjusting the band characteristics to utilize more portion of the solar energy.

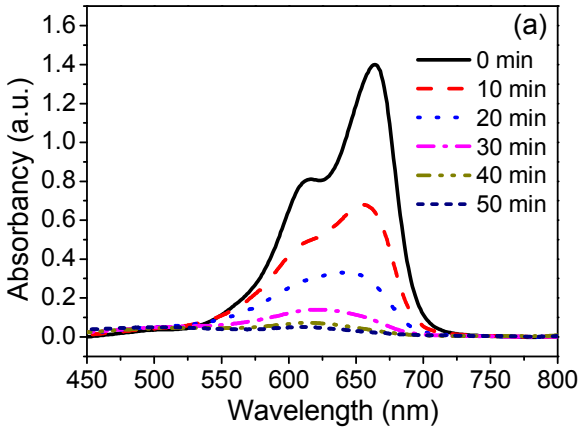

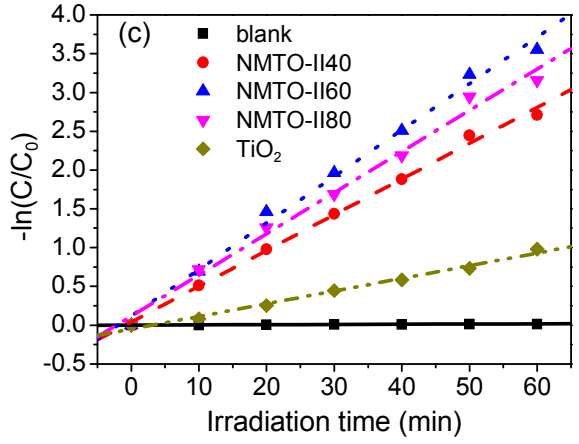

Fig. 6. (a) Temporal absorption spectral changes of MB in the presence of NMTO-II40 under simulated sunlight irradiation; (b) photocatalytic degradation of MB in an aqueous solution over the NMTO powers synthesized by reduction of 12% MgO, as well as TiO_2 raw material; (c) $\ln(C_0/C)$ versus UV–vis irradiation time in the presence of samples.

Adsorption-desorption

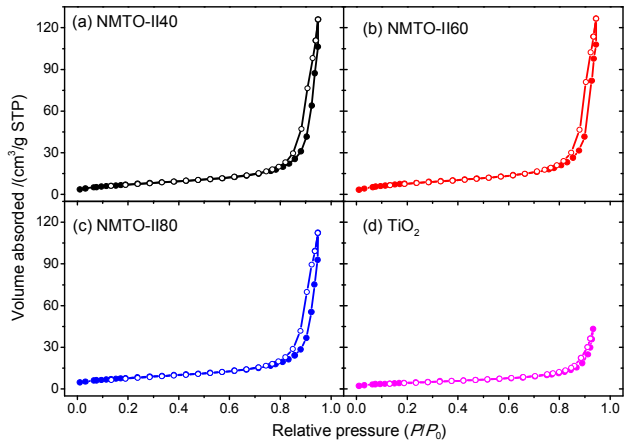

Fig. 7. Nitrogen adsorption-desorption isotherms of (a) NMTO-II40, (b) NMTO-II60, (c) NMTO-II80 and (d) TiO_2 raw material.

The specific surface area of the samples was measured to understand the photocatalytic activity deeply. The surface area was characterized by using the BET method with nitrogen adsorption-desorption at 77 K. Fig. 7 displays the adsorption-desorption isotherms of NMTO-II samples as well as TiO_2 raw powder, which can be classified as type II with hysteresis loops, indicating a typical nano crystalline structures, keeping consistent with the HRTEM results in Fig. 2. It was calculated that the specific surface area of NMTO-II40, NMTO-II60, NMTO-II80 and TiO_2 are 26.60, 30.36, 28.59 and 16.29 m^2/g as listed in Table 1. Although there is still much argument in whether the photocatalytic activity can be directly related to the catalyst surface area, it was generally believed that the adsorption on the catalyst surface would help to concentrate the reactant molecules for photoreactions and the photos might be scattered between the nano particles. Also, the photogenerated electrons and holes as well as the adsorbed molecules might diffuse more easily on the surface of catalyst with small particle size, causing the easy photoreactions.[31] Therefore, the photocatalyst with higher BET surface usually enjoys higher photocatalytic activity.

We further evaluated the photocatalytic performance of the samples on MB with parameter k/S_{BET} [$g/(m^2 \cdot min)$]. The parameter k/S_{BET} can eliminate the influence of BET surface and reveal the natural photocatalytic property of materials. The strongest photocatalyst is still NMTO-I60 even under consideration of surface area as listed in Table 1. The MB photodegradation over the samples are two times higher than that of TiO_2 based on the data in Table 1.

Mechanisms for the MB photodegradation over NMTO

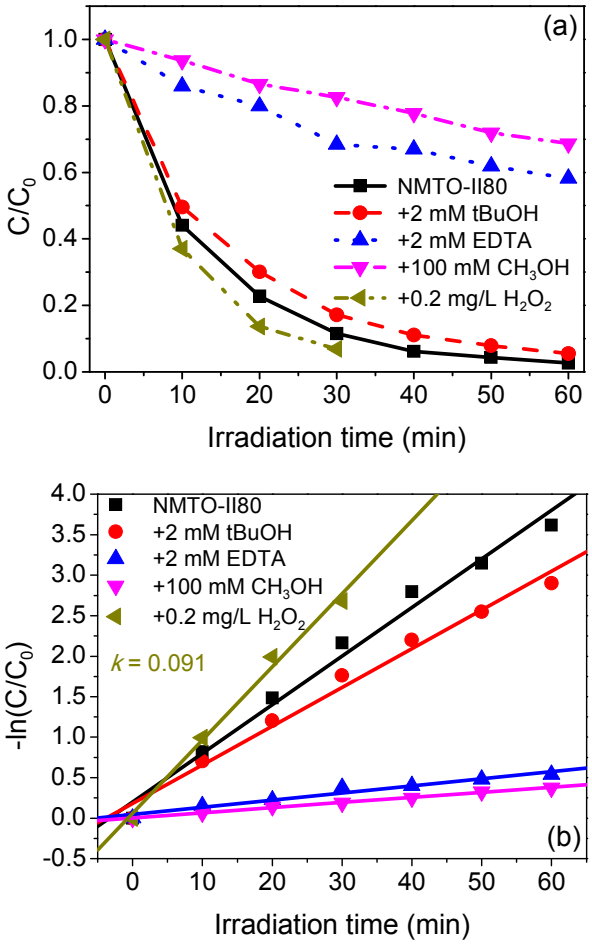

Fig. 8. (a) Effect of scavengers EDTA, tBuOH, CH_3OH and H_2O_2 on the photocatalytic degradation of MB over NMTO-II80 powers; (b) $\ln(C_0/C)$ versus UV–vis irradiation time in the presence of samples.

The activated species for photooxidation of dyes mainly include superoxide radicals, hydroxyl radicals and photogenerated holes. The oxidative species generated in the photocatalytic process can be discriminated through trapping experiments of holes, hydroxyl radicals and oxygen by adding ethylenediaminetetraacetic acid (EDTA), tert-butyl alcohol (tBuOH) and methanol, respectively.[32,33] Experiments were repeated by adding 2 mM EDTA, 2 mM tBuOH or 100 mM CH_3OH for NMTO-II80. Fig. 8 shows the photocatalytic degradation of MB over NMTO-II80 with different additives. The presence of tBuOH acted as

hydroxyl radical scavenger leads to a little suppression on the profile of MB degradation, and the pseudo-first order rate slightly decreases from 0.06 min^{-1} to 0.05 min^{-1}. But the degradation is evidently depressed with the presence of hole scavenger EDTA (k = 0.0088 min^{-1}). Therefore, the photogenerated holes on catalyst surface are the major active species participating in the degradation process, even though the reactive hydroxyl radicals are responsible species for part of the photocatalytic oxidation reaction. And the degradation is more notorious in the presence of 100 mM methanol acted as oxygen scavenger. Oxygen efficiently inhibits the recombination of photoinduced electron-hole pairs by reaction with electrons,[34] resulting in more long-lived holes participating in the oxidation reaction. Conversely, the photocatalytic degradation of MB is significantly improved by adding 0.2 mg/L H_2O_2 (k = 0.091 min^{-1}) as shown in Fig. 8, confirming the oxygen effect of prolonging the lifetime of electron-hole pairs.

Then, a mechanism for the degradation of organic compounds MB over NMTO under UV-visible light is proposed on the basis of above experimental results. The process of photoreaction equations are described as follows:

$$\mathrm{NMTO} + h\nu \rightleftharpoons \mathrm{NMTO} + (h^+_{v.b.} + e^-_{c.b.}) \quad (3)$$

$$e^-_{c.b.} + O_2 \rightarrow \cdot O_2^- \quad (4)$$

$$\cdot O_2^- + H^+ \rightarrow H_2O_2 + O_2 \quad (5)$$

$$H_2O_2 + e^-_{c.b.} \rightarrow \cdot OH + OH^- \quad (6)$$

$$h^+_{v.b.} + OH^- \rightarrow \cdot OH \quad (7)$$

$$h^+_{v.b.} + H_2O \rightarrow H^+ + \cdot OH \quad (8)$$

$$MB + h\nu \longrightarrow MB^* \quad (9)$$

$$MB^* + \mathrm{NMTO} \rightarrow \cdot MB^+ + \mathrm{NMTO}(e^-_{c.b.}) \quad (10)$$

$$O_2 + \mathrm{NMTO}(e^-_{c.b.}) \rightarrow \cdot O_2^- \quad (11)$$

$$\cdot MB^+ + (\cdot OH,\ \cdot O_2^-,\ O_2) \rightarrow \text{degradation products} \quad (12)$$

$$MB + h^+_{v.b.} \rightarrow \text{degradation products} \quad (13)$$

The electron-hole pair is photogenerated when an electron in NMTO is excited from the valence band to the conduction band after absorbing a photon with energy greater than 3.55 eV [reaction (3)]. The direct band of NMTO is helpful for the photon absorption and electron transition. The generated electrons and holes migrate to the surface of NMTO nanosheets. Then, the electrons are captured by the dissolved oxygen in the solution to generate $\cdot O_2^-$ radicals [reaction (4)]. These $\cdot O_2^-$ radicals can react with H^+ ions to produce H_2O_2 [reaction (5)], following on capturing a photogenerated electron and converting to ·OH and OH^- radicals [reaction (6)] to degrade MB. The ·OH can be also produced through the hole oxidation of OH^- or H_2O [reactions (7) and (8)]. MB is considered as a photosensitizer in the photosensitization pathway. It is excited to singlet or triplet state after absorbing the light energy and is signed as MB^* [reactions (9)]. Subsequently, the electron injects from excited dye molecule into NMTO conductor band and reacts with O_2 to generate $\cdot O_2^-$ [reactions (10) and (11)]. The cationic dye $\cdot MB^+$ radicals can react with reactive oxygen/hydroxyl radicals to generate intermediates that lead to degradation [reactions (12)].

The reaction (4) is an important process, which enhances the hole lifetime by absorbing electrons to suppress the electron-hole pair recombination. The separated electron-hole pairs are available for oxidation-reduction reactions. The presence of H_2O_2 also inhibits the electron-hole pair recombination due to the reaction (6), and hence significantly improves the MB photodegradation rate as shown in Fig. 8. Finally, the holes oxidize the adsorbed organic pollutants to yield the degradation products [reaction (13)], which is the major process in the MB photodegradation. Fig. 9 shows the band structure schematic and the possibly photoreaction on the surface of NMTO.

The hydroxyl radicals are the predominant active species that can oxidize the adsorbed organic pollutants in the MB photodegradation over some photocatalysts,[35,36] but for our sample NMTO, photogenerated holes play a major role in the MB photodegradation based on the above discussion.

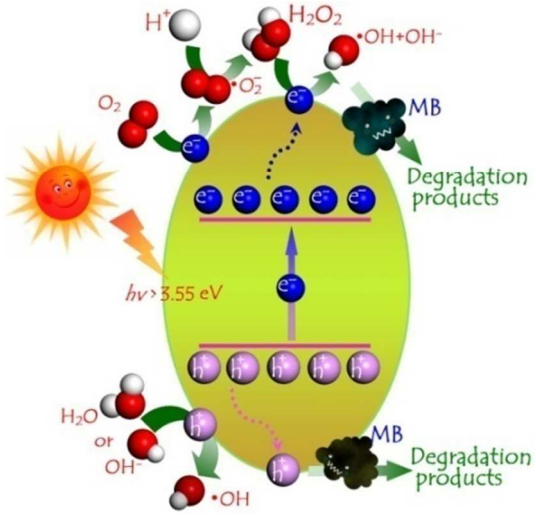

Fig. 9. Band structure schematic of NMTO and possible reaction for degradation of organic compounds MB over NMTO.

Conclusions

In summary, highly crystallized NMTO nanosheets with dominant {0 0 1} facets were synthesized by a simple hydrothermal method. This new-type semiconductor was demonstrated as a direct bandgap semiconductor with a bandgap of about 3.55 eV, which was helpful for absorbing photons. The photocatalytic activity of the NMTO nanosheets was evaluated by photodegrading MB under UV-visible light irradiation. NMTO exhibits higher photodegradation ability in comparison with the other similar pure photocatalyst even considering the surface area. The photogenerated holes are mainly responsible for the MB photodegradation according to the trapping experiments.

Thus, the presence of H_2O_2 evidently enhances the NMTO photodegradation ability by suppressing the electron-hole recombination through capturing the photogenerated electrons. NMTO exhibits strong photodegradation ability though its large band gap limits the utilization of solar energy. We believe that the heterostructure based on NMTO is one of the promising photocatalysts.

Acknowledgements

Financial support from the National Natural Science Foundation of China (Grand Nos.: 51172138 and 51372148) and Fundamental Research Funds for the Central Universities (Grand No.: GK201401003).

Notes and references

[a] *School of Physics and Information Technology, Shaanxi Normal University, Xi'an 710062, People's Republic of China. Fax: +86-29-81530750; Tel: +86-29-85303823; E-mail: zhoujp@snnu.edu.cn*
[b] *School of Materials Science and Engineering, Shaanxi Normal University, Xi'an, 710062, People's Republic of China.*
[c] *Department of Electronic Science, Key Laboratory of Functional Composite Materials of Guizhou Province, Guizhou University, Guiyang, 550025, People's Republic of China*

References

1. H. Xu, S. Ouyang, L. Liu, P. Reunchan, N. Umezawa and J. Ye, *J. Mater. Chem. A*, 2014, **2**, 12642.
2. H. Zhang, G. Chen and D. W. Bahnemann, *J. Mater. Chem.*, 2009, **19**, 5089.
3. H. G. Yang, C. H. Sun, S. Z. Qiao, J. Zou, G. Liu, S. C. Smith, H. M. Cheng and G. Q. Lu, *Nature*, 2008, **453**, 638.
4. M. Lazzeri, A. Vittadini and A. Selloni, *Phys. Rev. B*, 2001, **63**, 155409.
5. S. Liu, J. Yu and M. Jaroniec, *J. Am. Chem. Soc.*, 2010, **132**, 11914.
6. J. Pan, G. Liu, G. Q. Lu and H. M. Cheng, *Angew. Chem. Int. Edit.*, 2011, **50**, 2133.
7. N. Wu, J. Wang, D. N. Tafen, H. Wang, J.-G. Zheng, J. P. Lewis, X. Liu, S. S. Leonard and A. Manivannan, *J. Am. Chem. Soc.*, 2010, **132**, 6679.
8. J. S. Chen, Y. L. Tan, C. M. Li, Y. L. Cheah, D. Luan, S. Madhavi, F. Y. C. Boey, L. A. Archer and X. W. Lou, *J. Am. Chem. Soc.*, 2010, **132**, 6124.
9. H. B. Jiang, Q. Cuan, C. Z. Wen, J. Xing, D. Wu, X. Q. Gong, C. Li and H. G. Yang, *Angew. Chem. Int. Edit.*, 2011, **50**, 3764.
10. F. Zuo, K. Bozhilov, R. J. Dillon, L. Wang, P. Smith, X. Zhao, C. Bardeen and P. Feng, *Angewandte Chemie*, 2012, **124**, 6327.
11. S. Tominaka, Y. Tsujimoto, Y. Matsushita and K. Yamaura, *Angew. Chem. Int. Edit.*, 2011, **50**, 7418.
12. Z. Xiong and X. S. Zhao, *J. Am. Chem. Soc.*, 2012, **134**, 5754.
13. N. Feng, Q. Wang, A. Zheng, Z. Zhang, J. Fan, S.-B. Liu, J.-P. Amoureux and F. Deng, *J. Am. Chem. Soc.*, 2013, **135**, 1607.
14. Q. Zhang, D. Q. Lima, I. Lee, F. Zaera, M. Chi and Y. Yin, *Angew. Chem. Int. Edit.*, 2011, **50**, 7088.
15. R. Asahi, T. Morikawa, T. Ohwaki, K. Aoki and Y. Taga, *Science*, 2001, **293**, 269.
16. A. E. Nogueira, E. Longo, E. R. Leite and E. R. Camargo, *J. Colloid Interf. Sci*, 2014, **415**, 89.
17. O. Merka, D. W. Bahnemann and M. Wark, *Catal. Today*, 2014, **225**, 102.
18. Y. Wang, L. Liu, L. Xu, C. Meng and W. Zhu, *J. Appl. Phys.*, 2013, **113**, 174311.
19. A. Pearson, H. Jani, K. Kalantar-zadeh, S. K. Bhargava and V. Bansal, *Langmuir.*, 2011, **27**, 6661.
20. G. Lui, J.-Y. Liao, A. Duan, Z. Zhang, M. Fowler and A. Yu, *J. Mater. Chem. A*, 2013, **1**, 12255.
21. V. B. Nalbandyan, S. I. Rykalova, E. A. Bikyashev and S. Y. Isakova, *Russ. J. Inorg. Chem*+. 1989, **34**, 1356.
22. J. F. Moulder and J. Chastain, *Handbook of X-ray Photoelectron Spectroscopy: A Reference Book of Standard Spectra for Identification and Interpretation of XPS Data*, Physical Electronics Division, Perkin-Elmer Corporation, 1992.
23. H. He, J. Yin, Y. Li, Y. Zhang, H. Qiu, J. Xu, T. Xu and C. Wang, *Appl. Catal. B: Environ*, 2014, **156-157**, 35.
24. J. Pan, X. Wu, L. Wang, G. Liu, G. Q. Lu and H. M. Cheng, *Chem. Commun.*, 2011, **47**, 8361.
25. S. Ge, B. Wang, D. Li, W. Fa, Z. Yang, Z. Yang, G. Jia and Z. Zheng, *Appl. Surf. Sci.*, 2014, **295**, 123.
26. M. A. Butler, *J. Appl. Phys.*, 1977, **48**, 1914.
27. R. López and R. Gómez, *J. Sol-gel. Sci. Techn.*, 2011, **61**, 1.
28. S. N. Hosseini, S. M. Borghei, M. Vossoughi and N. Taghavinia, *Appl. Catal. B: Environ*, 2007, **74**, 53.
29. R. Talling, R. Dashwood, M. Jackson, S. Kuramoto and D. Dye, *Scripta Materialia*, 2008, **59**, 669.
30. S. Shamaila, A. K. L. Sajjad, F. Chen and J. Zhang, *Journal of colloid and interface science*, 2011, **356**, 465.
31. J.-F. Guo, B. Ma, A. Yin, K. Fan and W.-L. Dai, *Appl. Catal. B: Environ*, 2011, **101**, 580.
32. C. Minero, G. Mariella, V. Maurino, D. Vione and E. Pelizzetti, *Langmuir.*, 2000, **16**, 8964.
33. N. Serpone, I. Texier, A. V. Emeline, P. Pichat, H. Hidaka and J. Zhao, *J. Photoch. Photobio. A*, 2000, **136**, 145.
34. C. Pan and Y. Zhu, *Environmental science & technology*, 2010, **44**, 5570.
35. L. Sun and J. R. Bolton, *The Journal of Physical Chemistry*, 1996, **100**, 4127.
36. L. G. Devi and R. Kavitha, *Appl. Catal. B: Environ*, 2013, **140-141**, 559.

Manuscript title: A new-type semiconductor $Na_{0.9}Mg_{0.45}Ti_{3.55}O_8$: preparation, characterization and photocatalysis

By Ze-Qing Guo, Jian-Ping Zhou, Long-Liang An, Jia-Xing Jiang, Gang-Qiang Zhu, Chao-Yong Deng

$Na_{0.9}Mg_{0.45}Ti_{3.55}O_8$ single crystal nanosheets with dominant {0 0 1} facets exhibit strong photodegradation ability for methylene blue under UV-visible light.